Available online at www.sciencedirect.com
SCIENCE DIRECT®
Astroparticle Physics 21 (2004) 223–240
Astroparticle Physics
www.elsevier.com/locate/astropart

The cosmic ray proton, helium and CNO fluxes in the 100 TeV energy region from TeV muons and EAS atmospheric Cherenkov light observations of MACRO and EAS-TOP

EAS-TOP Collaboration

M. Aglietta [a], B. Alessandro [b], P. Antonioli [c], F. Arneodo [d], L. Bergamasco [e], M. Bertaina [e,f,*], C. Castagnoli [g], A. Castellina [a], A. Chiavassa [e], G. Cini [e], B. D'Ettorre Piazzoli [h], G. Di Sciascio [h], W. Fulgione [a], P. Galeotti [e], P.L. Ghia [a], M. Iacovacci [h], G. Mannocchi [a], C. Morello [a], G. Navarra [e], O. Saavedra [e], A. Stamerra [e,i], G.C. Trinchero [a], S. Valchierotti [e], P. Vallania [a], S. Vernetto [a], C. Vigorito [e]

MACRO Collaboration

M. Ambrosio [h], R. Antolini [d], A. Baldini [j], G.C. Barbarino [h], B.C. Barish [k], G. Battistoni [l,m], Y. Becherini [n], R. Bellotti [o], C. Bemporad [j], P. Bernardini [p], H. Bilokon [l], C. Bower [q], M. Brigida [o], S. Bussino [r], F. Cafagna [o], M. Calicchio [o], D. Campana [h], M. Carboni [l], R. Caruso [s], S. Cecchini [n,t], F. Cei [j], V. Chiarella [l], T. Chiarusi [n], B.C. Choudhary [k], S. Coutu [u,v], M. Cozzi [n], G. De Cataldo [o], H. Dekhissi [n,w], C. De Marzo [o], I. De Mitri [p], J. Derkaoui [n,w], M. De Vincenzi [r], A. Di Credico [d], O. Erriquez [o], C. Favuzzi [o], C. Forti [l], P. Fusco [o], G. Giacomelli [n], G. Giannini [j,x], N. Giglietto [o], M. Giorgini [n], M. Grassi [j], A. Grillo [d], F. Guarino [h], C. Gustavino [d], A. Habig [y,z], K. Hanson [u], R. Heinz [q], E. Iarocci [l,aa], E. Katsavounidis [k,ab], I. Katsavounidis [k,ac], E. Kearns [y], H. Kim [k], S. Kyriazopoulou [k], E. Lamanna [ad,ae], C. Lane [af], D.S. Levin [u], P. Lipari [ad], N.P. Longley [k,ag], M.J. Longo [u], F. Loparco [o], F. Maaroufi [n,w], G. Mancarella [p], G. Mandrioli [n], A. Margiotta [n], A. Marini [l], D. Martello [p], A. Marzari-Chiesa [ah], M.N. Mazziotta [o], D.G. Michael [k], P. Monacelli [s], T. Montaruli [o],

[*] Corresponding author. Tel.: +39-011-6707350; fax: +39-011-6707493.
E-mail address: bertaina@to.infn.it (M. Bertaina).

0927-6505/$ - see front matter
doi:10.1016/j.astropartphys.2004.01.005

M. Monteno [ah], S. Mufson [q], J. Musser [q], D. Nicolò [j], R. Nolty [k], C. Orth [y], G. Osteria [h], O. Palamara [d], V. Patera [l,aa], L. Patrizii [n], R. Pazzi [j], C.W. Peck [k], L. Perrone [p], S. Petrera [s], V. Popa [n,ai], A. Rainò [o], J. Reynoldson [d], F. Ronga [l], C. Satriano [ad,aj], E. Scapparone [d], K. Scholberg [y,ab], A. Sciubba [l,aa], M. Sioli [n], G. Sirri [n], M. Sitta [ah,ak], P. Spinelli [o], M. Spinetti [l], M. Spurio [n], R. Steinberg [af], J.L. Stone [y], L.R. Sulak [y], A. Surdo [p], G. Tarlé [u], V. Togo [n], M. Vakili [al,am], C.W. Walter [y], R. Webb [am]

[a] *Istituto di Fisica dello Spazio Interplanetario del CNR, Sezione di Torino 10133 Torino, and INFN, 10125 Torino, Italy*
[b] *INFN, Sezione di Torino 10125 Torino, Italy*
[c] *INFN, Sezione di Bologna 40126 Bologna, Italy*
[d] *Laboratori Nazionali del Gran Sasso dell'INFN, 67010 Assergi (L'Aquila), Italy*
[e] *Dipartimento di Fisica Generale dell'Università di Torino and INFN, 10125 Torino, Italy*
[f] *Istituto Tecnico Industriale "G. Vallauri", 12045 Fossano (Cuneo), Italy*
[g] *Istituto di Fisica dello Spazio Interplanetario del CNR, Sezione di Torino 10133 Torino, and Dipartimento di Fisica Generale dell'Università di Torino, 10125 Torino, Italy*
[h] *Dipartimento di Fisica dell'Università di Napoli and INFN, 80125 Napoli, Italy*
[i] *Dipartimento di Fisica dell'Università di Siena and INFN, 53100 Siena, Italy*
[j] *Dipartimento di Fisica dell'Università di Pisa and INFN, 56010 Pisa, Italy*
[k] *California Institute of Technology, Pasadena, CA 91125, USA*
[l] *Laboratori Nazionali di Frascati dell'INFN, 00044 Frascati (Roma), Italy*
[m] *INFN Milano, 20133 Milano, Italy*
[n] *Dipartimento di Fisica dell'Università di Bologna and INFN, 40126 Bologna, Italy*
[o] *Dipartimento di Fisica dell'Università di Bari and INFN, 70126 Bari, Italy*
[p] *Dipartimento di Fisica dell'Università di Lecce and INFN, 73100 Lecce, Italy*
[q] *Departments of Physics and of Astronomy, Indiana University, Bloomington, IN 47405, USA*
[r] *Dipartimento di Fisica dell'Università di Roma Tre and INFN Sezione Roma Tre, 00146 Roma, Italy*
[s] *Dipartimento di Fisica dell'Università dell'Aquila and INFN, 67100 L'Aquila, Italy*
[t] *Istituto TESRE/CNR, 40129 Bologna, Italy*
[u] *Department of Physics, University of Michigan, Ann Arbor, MI 48109, USA*
[v] *Department of Physics, Pennsylvania State University, University Park, PA 16802, USA*
[w] *L.P.T.P, Faculty of Sciences, University Mohamed I, B.P. 524 Oujda, Morocco*
[x] *Università di Trieste and INFN, 34100 Trieste, Italy*
[y] *Physics Department, Boston University, Boston, MA 02215, USA*
[z] *Duluth Physics Department, University of Minnesota, Duluth, MN 55812, USA*
[aa] *Dipartimento di Energetica, Università di Roma, 00185 Roma, Italy*
[ab] *Department of Physics, MIT, Cambridge, MA 02139, USA*
[ac] *Intervideo Inc., Torrance, CA 90505, USA*
[ad] *Dipartimento di Fisica dell'Università di Roma "La Sapienza" and INFN, 00185 Roma, Italy*
[ae] *Dipartimento di Fisica dell'Università della Calabria, 87036 Rende (Cosenza), Italy*
[af] *Department of Physics, Drexel University, PA 19104, USA*
[ag] *Department of Physics and Astronomy, Macalester College, St. Paul, MN 55105, USA*
[ah] *Dipartimento di Fisica Sperimentale dell'Università di Torino and INFN, 10125 Torino, Italy*
[ai] *Institute for Space Sciences, 76900 Bucharest, Romania*
[aj] *Università della Basilicata, 85100 Potenza, Italy*
[ak] *Dipartimento di Scienze e Tecnologie Avanzate, Università del Piemonte Orientale, 15100 Alessandria, Italy*
[al] *Resonance Photonics, Markham, Ont., Canada*
[am] *Physics Department, Texas A&M University, College Station, TX 77843, USA*

Received 22 October 2003; received in revised form 14 January 2004; accepted 26 January 2004
Available online 26 February 2004

Abstract

The primary cosmic ray (CR) proton, helium and CNO fluxes in the energy range 80–300 TeV are studied at the National Gran Sasso Laboratories by means of EAS-TOP (Campo Imperatore, 2005 m a.s.l.) and MACRO (deep underground, 3100 m w.e., the surface energy threshold for a muon reaching the detector being $E_{\mu}^{\rm th} \approx 1.3$ TeV). The measurement is based on: (a) the selection of primaries based on their energy/nucleon (i.e., with energy/nucleon sufficient to produce a muon with energy larger than 1.3 TeV) and the reconstruction of the shower geometry by means of the muons recorded by MACRO in the deep underground laboratories; (b) the detection of the associated atmospheric Cherenkov light (C.l.) signals by means of the C.l. detector of EAS-TOP. The C.l. density at core distance $r > 100$ m is directly related to the total primary energy E_0. Proton and helium ("p + He") and proton, helium and CNO ("p + He + CNO") primaries are thus selected at $E_0 \simeq 80$ TeV, and at $E_0 \simeq 250$ TeV, respectively. Their flux is measured: $J_{\rm p+He}(80\ {\rm TeV}) = (1.8 \pm 0.4) \times 10^{-6}$ m^{-2} s^{-1} sr^{-1} TeV^{-1}, and $J_{\rm p+He+CNO}(250\ {\rm TeV}) = (1.1 \pm 0.3) \times 10^{-7}$ m^{-2} s^{-1} sr^{-1} TeV^{-1}, their relative weights being: $\frac{J_{\rm p+He}}{J_{\rm p+He+CNO}}(250\ {\rm TeV}) = 0.78 \pm 0.17$. By using the measurements of the proton spectrum obtained from the direct experiments and hadron flux data in the atmosphere, we obtain for the relative weights of the three components at 250 TeV: $J_{\rm p} : J_{\rm He} : J_{\rm CNO} = (0.20 \pm 0.08) : (0.58 \pm 0.19) : (0.22 \pm 0.17)$. This corresponds to the dominance of helium over proton primaries at 100–1000 TeV, and a possible non-negligible contribution from CNO.

The lateral distribution of Cherenkov light in Extensive Air Showers (EASs), which is related to the rate of energy deposit of the primary in the atmosphere, is measured for a selected proton and helium primary beam, and good agreement is found when compared with the one calculated with the CORSIKA/QGSJET simulation model.

PACS: 96.40.Pq; 96.40.De; 29.40.Ka; 98.70.Sa
Keywords: Cosmic rays; Composition; High energies; Extensive air showers; Underground muons

1. Introduction

The knowledge of the energy spectrum of the different elements of the primary cosmic rays is a main tool for understanding the acceleration processes and the cosmic ray sources. In the energy region accessible to direct measurements (obtained through detectors operating on balloons and satellites), the information on cosmic ray primaries is quite reliable, while approaching 100 TeV it becomes less so since the statistics become poor, and the energy determinations, being non-calorimetric, depend on the interaction parameters and their fluctuations.

In the highest energy range accessible to direct measurements a difference is observed between the proton and heavy nuclei spectra (the power indices of the energy spectra being: $\gamma_{\rm p} \approx 2.8$ vs. $\gamma_{\rm CNO,Fe} \approx 2.5$–$2.6$) [1–3]. Different spectra could be due to a rigidity limit of the acceleration process or to different mechanisms and sites for acceleration of protons and heavier nuclei ([4,5], and references therein).

The question of the consistency of the proton and heavier nuclei spectra was raised a long time ago [6,7]. The situation is experimentally not yet defined because the most recent data by direct experiments (JACEE [8] and RUNJOB [9]) are consistent with each other for the proton ($\gamma_{\rm p} \approx 2.8$) and for the medium–heavy elements spectra ($\gamma_{\rm CNO} \approx \gamma_{\rm Fe} \approx 2.5$–$2.6$), while they do not agree on the helium one ($\gamma_{\rm He} \approx \gamma_{\rm p}$ for RUNJOB, while $\gamma_{\rm He} \approx \gamma_{\rm CNO,Fe}$ for JACEE). Preliminary data on the proton and helium spectra from the very recent ATIC experiment [10] have not been able to settle the question yet. In particular, such different spectra lead to a primary beam dominated above 100 TeV by either helium or heavier primaries (or even protons if the spectral slopes of all primaries are equal). Beside the difficulties in the interpretation deriving from such uncertainty, the problem is relevant for EAS observations in the "knee" region, for which a sound starting point at the lowest energies would be of great importance.

A study of the proton, helium and CNO fluxes in the energy range 80–300 TeV was done at the

National Gran Sasso Laboratories with a ground based experiment, EAS-TOP (at mountain altitude, 2005 m a.s.l.) and MACRO deep underground (3100 m w.e., the surface energy threshold for a muon reaching the detector being $E_\mu^{th} \approx 1.3$ TeV). Due to their locations the two arrays allow the simultaneous detection of the high energy muons, and of the e.m. and Cherenkov light components of Extensive Air Showers [11,12]. The technique is based on:

- The selection of air shower events through the TeV muon recorded by MACRO. The primaries are selected on the basis of their energy/nucleon by means of the TeV muon information. The underground muons further provide the EAS core geometry: core location and arrival direction, with precisions of about 20 m and 1°, respectively.
- The measurement of the Cherenkov light intensity, which is related to the total primary energy, and of the average C.l. lateral distribution at the surface, by means of the C.l. detectors of the EAS-TOP array. The surface array operates at an energy threshold E_0^{th} of 40 TeV at an EAS core distance r of 130 m.

Due to the shower selection through the high energy muons ($E_\mu \gtrsim 1.3$ TeV to reach the underground detector) at the total energy threshold (E_0^{th}) the selected primaries are mainly protons. For $E_o > 40$ TeV, they include both protons and helium nuclei. CNO primaries contribute significantly at energies $E_o > 100$ TeV (the contribution of each primary becoming significant for $A \cdot E_\mu / E_0^{th} \approx 0.1$ to 0.2, see Section 4.2). The combined geometric factors and life times of the two detectors provide a total acceptance A_c of 20,000 h m^2 sr.

A ground based measurement of the primary proton flux over a wide energy range (0.5–50 TeV), inferred from the locally measured hadron spectrum, has been reported by the EAS-TOP Collaboration [13], resulting in very good agreement with the direct measurements ($\gamma_p \approx 2.8$). The present experiment provides a measurement of the "proton + helium" flux at 80 TeV and of the "proton + helium + CNO" one at 250 TeV. By using the measured proton flux, the helium and CNO contributions are obtained. Moreover, while the event rate is related to the cosmic ray flux, the shape of the lateral distribution of Cherenkov light is mainly related to the rate of energy release in the atmosphere and therefore to the properties of the hadron interactions. The model used for their description can therefore be checked with a rather "pure" (by the standards of EAS observations) proton, helium and CNO (over 100 TeV) primary beam. From such a point of view, the present measurement therefore provides a verification of the tools used for the analysis of Extensive Air Shower data at higher energies. The reported measurement of the C.l. intensity and lateral distribution for a given primary beam validates the simulations used, e.g., in TeV gamma-ray astronomy applications.

We will present and discuss here:

(a) the experimental arrays, and the data reduction;
(b) the method of analysis and the general results of the observation;
(c) the measured Cherenkov light lateral distribution and its comparison with the expectations from a simulation code based on CORSIKA/QGSJET;
(d) the measured contributions to the primary spectrum of the helium and CNO primaries and a comparison with expectations from extrapolations of the primary spectra reported by direct measurements.

2. The detectors

EAS-TOP [14] is a multicomponent Extensive Air Shower array operating at Campo Imperatore (2005 m a.s.l.), at an average zenith angle of 35° with respect to the vertical of the underground Gran Sasso laboratories, and including detectors of the electromagnetic [15], muon [16], hadron [17] and atmospheric Cherenkov light [18] components.

The Cherenkov light (C.l.) array of EAS-TOP consists of 5 telescopes 60–80 m apart, with their optical axis aligned with the MACRO direction. Each telescope uses two wide angle detectors

equipped with 7 photomultipliers (PMTs) each with 6.8 cm photocathode diameter, where 1 is positioned in the center and 6 on a circular pattern at the focal plane of a parabolic mirror (0.5 m^2 effective collecting area, 40 cm focal length). The total field-of-view (f.o.v.) is 0.16 sr, the f.o.v. of each individual PMT being 2.3×10^{-2} sr. The two sets of 7 PMTs of each detector operate at voltages differing by about 200 V, providing High Gain (HG) and Low Gain (LG) channels to increase the dynamic range of the telescope and to check for possible nonlinearity effects.

Cherenkov light events are identified by the coincidence, in a time window of 30 ns, between any two PMTs with the same geometrical position on the focal plane of the two mirrors of the same telescope (referred to as "corresponding PMTs" in the following; the data from all PMTs are read out for every trigger). The trigger threshold is $N_{\rm phe}^{\rm th} = 120$ photoelectrons/PMT, corresponding to an energy threshold of $E_0^{\rm th} \approx 40$ TeV at a core distance of $r \approx 130$ m; the trigger rate is 7 Hz/telescope, and the dead time is 14% of the total life time.

MACRO [19], in the underground Gran Sasso Laboratory at 963 m a.s.l., 3100 m w.e. of minimum rock overburden, is a large area multipurpose apparatus designed to detect penetrating cosmic radiation. The detector has dimensions $76.6\times12\times4.8$ m^3. In this work, muon tracks with at least 4 aligned hits in both of the stereo views of the horizontal streamer tube planes (over the 10 layers composing the lower part of the detector) are considered. The angular resolution of the muon reconstructed direction is $\sigma_\theta = 0.95°$, domi- nated by multiple scattering in the rock overburden [19]. This, combined with the muon lateral spread at the surface and the lateral displacement due to the scattering in the rock (7 and 6.3 m, respectively, obtained with the simulation discussed in Section 4), leads to an uncertainty on the EAS core location at the level of EAS-TOP of $\sigma_r \approx 22$ m.

The two experiments are separated by a rock thickness ranging from 1100 up to 1300 m, depending on the angle (Fig. 1). The corresponding minimum energy for a muon to reach the depth of MACRO ranges from $E_\mu^{\rm th} \approx 1.3$ to $E_\mu^{\rm th} \approx 1.6$ TeV. EAS-TOP and MACRO have run in coincidence on clear moonless nights between September 1998 and May 2000 for a life time of $\Delta T = 208$ h. During this period, MACRO reconstructed 35,814 events in the angular field $16° < \theta < 58°$ and $127° < \phi < 210°$, corresponding to the region in zenith and azimuth angles seen by the Cherenkov telescopes. Event coincidence is established off-line, using two independent GPS clocks with accuracies of about 100 ns. 3830 events were found in coincidence with Cherenkov data in a time window $\Delta t = 7$ μs, the expected accidental contamination being 3.0 events (see Fig. 2). Since time measurements are absolute and independent, the positive shift observed in Fig. 2 represents the muon time-of-flight between the surface and the MACRO location, decreased by the longer time (about 1 μs) for trigger generation in EAS-TOP (geometrical differences, and fluctuations in trigger generation account for the fluctuations).

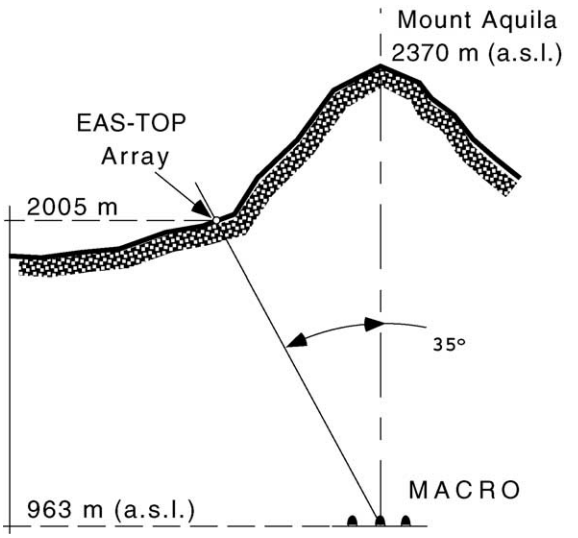

Fig. 1. Locations of the EAS-TOP and MACRO arrays at the National Gran Sasso Laboratories.

For further analysis, the muon coordinates (location and direction) as reconstructed by MACRO are used to localize the EAS core position and arrival direction at the surface, and therefore to identify the PMT to be used for the C.l. intensity measurement, and to determine the distance from the EAS core to each Cherenkov mirror. Due to the structure of the 7 PMTs in the focal plane (where the full field of view of each is 4.9° and the average displacement from the direct

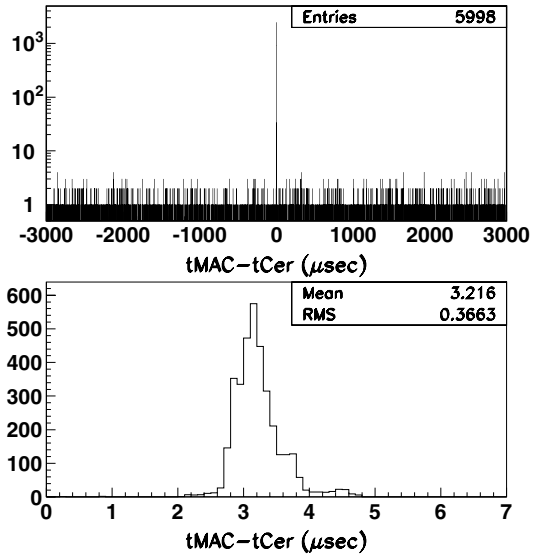

Fig. 2. Distribution of the temporal delays in coincident events using a window of $\Delta t = 6$ ms (top) or $\Delta t = 7$ μs (bottom).

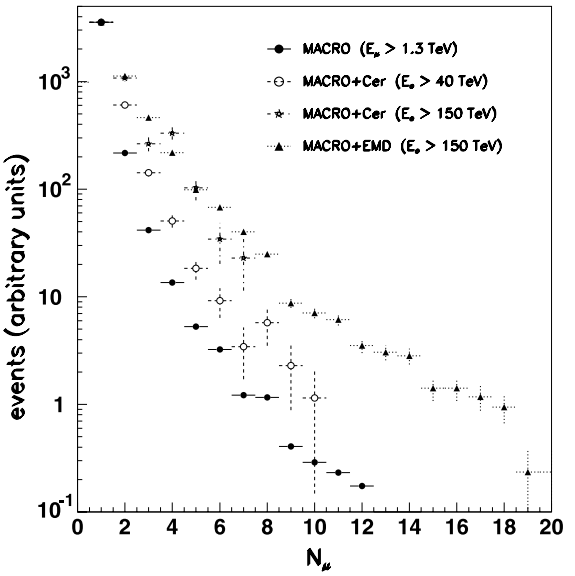

Fig. 3. Muon multiplicity distribution in MACRO events alone collected in the quoted angular and time window (see text) and in coincidence with Cherenkov and EMD detectors of EAS-TOP (the four sets of data are normalized to $N_\mu = 1$).

line of sight is 7°) and the relationship between core distance and angular scale at the surface (5.4°/100 m), EASs with core distances $r < 50$ and $125 < r < 185$ m can be analyzed, in the central PMT and in the external ones, respectively.

To illustrate the relation between the surface observation and the underground data, in Fig. 3 muon multiplicity distributions observed in MACRO for different conditions at the surface (corresponding to different primary energy thresholds) are shown for: (a) MACRO alone (primary energy $E_0 > 1.3$ TeV, i.e., muon energy threshold); (b) MACRO and EAS-TOP Cherenkov light detector ($E_0 > 40$ TeV); (c) MACRO and EAS-TOP Cherenkov light detector ($E_0 > 150$ TeV, selected from the Cherenkov light intensity); (d) MACRO in coincidence with the electromagnetic detector (EMD) of EAS-TOP ($E_0 > 150$ TeV) [11]. As expected, with increasing primary energy threshold, higher muon multiplicities are selected, and for similar primary energy thresholds obtained through either the e.m. or Cherenkov light detectors, the resulting muon multiplicity distributions are quite similar.

The reciprocal influence of the high energy muon triggering requirement on the C.l. signals is shown in Fig. 4, in which the recorded integral C.l.

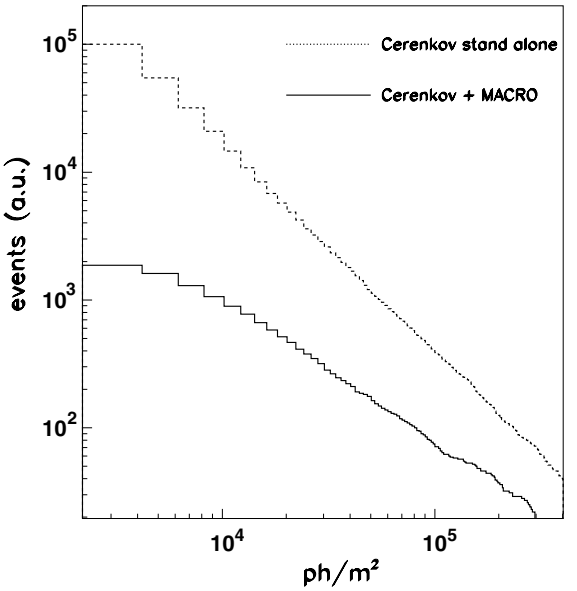

Fig. 4. Integral spectra of Cherenkov events recorded in standalone mode and in coincidence with MACRO. The coincidence spectrum is harder due to the larger muon numbers, and therefore triggering probability of MACRO, with increasing primary energy.

photon number spectra observed are shown in standalone mode and together with the MACRO trigger request. While the former has a slope $\gamma \approx 1.7$ reproducing, as expected, the primary cosmic ray spectrum, the latter is harder ($\gamma \approx 1.0$), where the difference in slope $\Delta\gamma \approx 0.7$ represents the increasing average muon number with primary energy, and therefore triggering probability of MACRO. It agrees with the calculated average relation: $\langle N_\mu \rangle \propto E_0^{0.7}$ [20].

3. Cherenkov light data reduction

The main points concerning the C.l. data treatment are summarized in the following.

Pedestal subtraction. The variable luminosity of the sky during a given night was taken into account by measuring and subtracting from the ADC readout the on-line pedestal, obtained every 300 s, as the charge value corresponding with the highest rate in each PMT spectrum (i.e., corresponding to the absence of any C.l. signal).

Long term variations (*including mirror reflectivity*). The number of photoelectrons (phe_{001}) corresponding to a fixed rate (0.01 Hz) where the detector is fully efficient was used to correct for long term variations. The dataset was divided into 3 subperiods and for each subperiod an average value ($\overline{phe_{001}}$) was calculated for each PMT. The average values for the second and third periods were normalized to that for the first one. After such a correction, the spread of the points represents the overall fluctuation of the detector response and of the environmental conditions, on a night by night basis from which we derive $\sigma_{\rm sky} \approx 15\%$. This value will be used also as a systematic uncertainty on the sky transparency.

PMT gains. The PMT gains were determined with a systematic uncertainty of $\sigma_{\rm g} \approx 12\%$ by using the single photoelectron technique. The central PMTs and separately the lateral ones were normalized to the same $\overline{phe_{001}}$ value; the width of such distributions is $\sigma_{\rm c} \approx 12\%$, confirming the above value of $\sigma_{\rm g}$.

Signal fluctuations. The fluctuations in the response of PMTs in single events were deduced from the comparison of the outputs of the HG and LG channels (corresponding PMTs). The systematic difference between the two channels is $\sigma(phe) = 13\%$, i.e., corresponding to the above uncertainty in PMT gain. The width of the distribution provides the uncertainty in individual measurements, that, as a function of the PMT signals, is given by

$$\left(\frac{\sigma(phe)}{phe}\right)^2 = (0.05 \pm 0.01)^2 + \frac{(3.1 \pm 0.2)^2}{phe}. \quad (1)$$

phe is the measured number of photoelectrons, which ranges between 200 and 2000.

Light collection efficiency and photon to photoelectron conversion. The geometric efficiency ($\epsilon_{\rm l}$) of the optical system in collecting the EAS C.l. (i.e., including the light collector response and the C.l. angular shape), as a function of the EAS geometry reconstructed from the MACRO muon data, was obtained with the simulation described in Section 4, and applied to each individual event. Only events with $\epsilon_{\rm l} > 50\%$ were used in the analysis. Fluctuations and uncertainties in the muon direction introduce an overall uncertainty of $\sigma_{\epsilon_{\rm l}} \approx 11\%$. The conversion from photoelectrons to photon numbers ($\epsilon = phe/ph$) was calculated by taking into account the mirror reflectivity ($\eta(\lambda)$) and the quantum efficiency ($\epsilon_{\rm q}(\lambda)$) of the photocathodes, resulting in $\epsilon\ (290 < \lambda < 630\ {\rm nm}) = 0.17$.

The sources of photon density uncertainties are shown in Table 1. An overall systematic uncertainty of $\sigma_{\rm sys} \approx 20\%$ is obtained. Concerning the statistical ones, the contributions of Table 1 and expression (1) should be added in quadrature.

Table 1
Summary of the different sources of uncertainty

Origin	Nature	Value (%)
Sky transparency	Syst.	15
PMTs' calibrations	Syst.	12–13
Night-to-night fluctuations	Stat.	15
Individual event light collection	Stat.	11

4. Simulations

The data were interpreted by means of simulations based on the CORSIKA code version 5.61

[21] and QGSJET [22] hadron interaction model. We summarize here their main results of relevance to the present analysis of Cherenkov light and high energy muons.

4.1. Cherenkov light

Protons, helium and carbon (for the CNO component) nuclei were generated as primary particles, with discrete energies between 20 and 300 TeV every 20–50 TeV (samples varying from about 1000 events at low energies to about 250 events at higher energies, in order that at least 100 events/sample be obtained in which a muon with energy $E_\mu > 1.3$ TeV is present). Zenith and azimuth angles were chosen randomly inside the telescopes' fields of view ($30° < \theta < 40°$ and $175° < \phi < 185°$). C.l. photons were selected in the range $290 < \lambda < 630$ nm. Atmospheric absorption was included following the CORSIKA package version 6.00 [23].

Two main aspects have to be considered when comparing the present results with other C.l. calculations: (a) the lateral distribution depends on the zenith angle, and therefore this has to be taken into account when comparing with the lateral distribution function (l.d.f.) usually obtained for vertical incidence (see Fig. 5(a)) and (b) the requirement of the presence of a muon with energy $E_\mu > 1.3$ TeV implies a reduction of the C. l. yield (see Fig. 5(b)) that amounts typically to about 20% at 80 TeV for primary protons.

The l.d.f.s for proton, helium and CNO primaries have similar shapes within 20% differences in intensity depending on energy (see Fig. 6).

To illustrate the extent of fluctuations of the photon density versus the core distance in Fig. 7 some l.d.f.s from 80 TeV proton showers are shown, and compared with the average one obtained from a 100 event sample. At small core distances, as measured with the central PMTs, the fluctuations are larger (mainly due to the correlation with the interaction height), and can be fitted with a Landau distribution. At larger distances ($r > 120$ m, measured with the lateral PMTs) the fluctuations are smaller, and better in agreement with gaussian shapes (Fig. 14). In this region the C. l. photon density is mainly related to the primary energy and therefore such events are selected

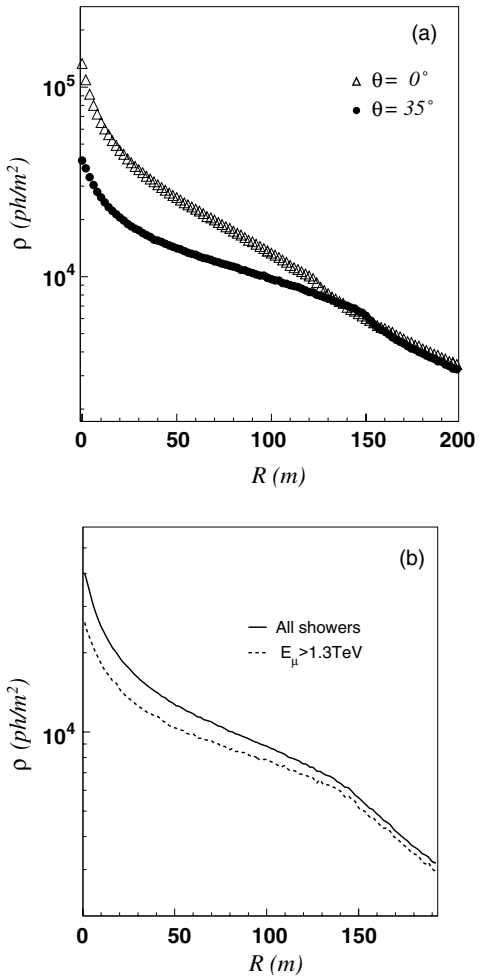

Fig. 5. (a) Dependence of the C. l. l.d.f. on the zenith angle for 80 TeV proton-initiated showers (0° and 35° zenith angles). (b) Average C. l. lateral distribution of 80 TeV proton primaries for all events (black line) and with the additional requirement of a muon with energy $E_\mu > 1.3$ TeV (dotted line); atmospheric absorption is not included.

for primary energy estimation. Numerical values obtained from the fits for the average values and fluctuations of the C. l. l.d.f. are given in Appendix A. The direct relation between primary energy and photon density at $r = 130$ m is shown in Fig. 8.

4.2. High energy muons

Proton, He, and C initiated showers with primary energy $E_0 > 1$ TeV were generated follo-

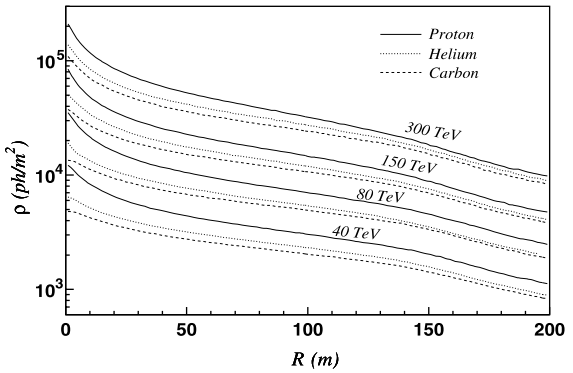

Fig. 6. C. l. lateral distributions for proton, helium, and carbon primaries of energies $E_0 = 40$, 80, 150, and 300 TeV, respectively.

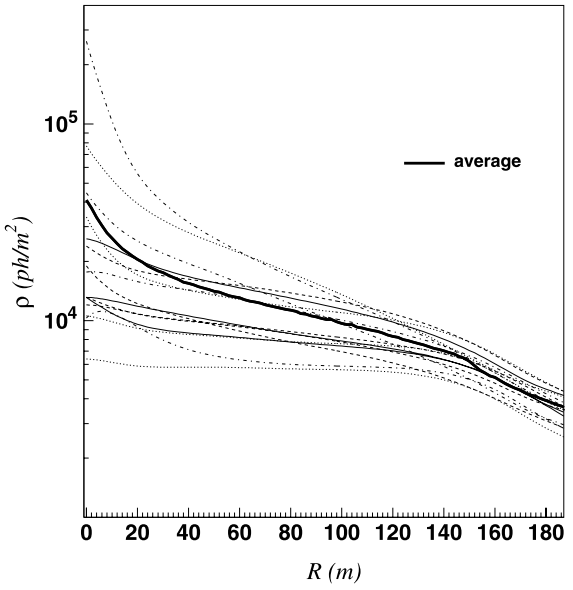

Fig. 7. Cherenkov photon density distribution for a sample of 14 simulated proton showers with 80 TeV. The average distribution based on 100 events is also shown as a full line.

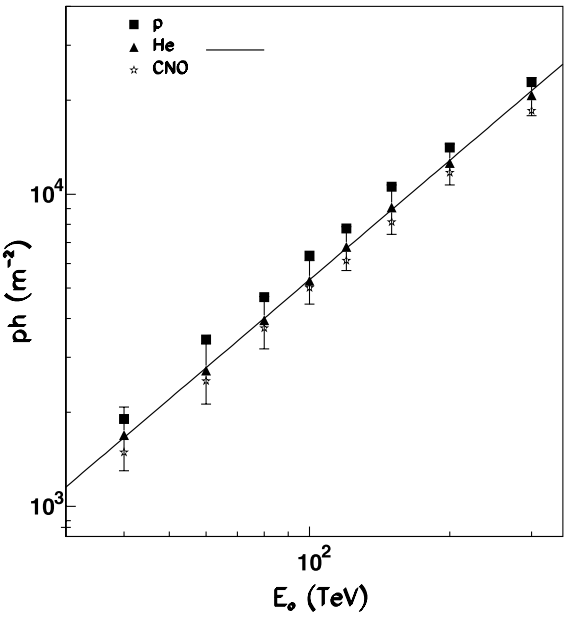

Fig. 8. Expected photon densities (ph/m^2) as a function of primary energy for $r = 130$ m for proton, helium and CNO primaries. The line represents the fit of expression (A.1). Error bars indicate the range of fluctuations in individual events.

wing the JACEE and RUNJOB spectra, as reported in Table 2. The statistical sample generated corresponds to about 1.4 times the amount of experimental data. Primary particles were sampled in a solid angle region on the order of the area encompassing the EAS-TOP array as seen from the underground detector. All muons with energy $E_\mu \geqslant 1$ TeV reaching the surface were propagated through the rock down to the MACRO depth by means of the muon transport code MUSIC [24].

The number of muons per event (N_μ) reaching the MACRO depth is shown in Fig. 9 together with

Table 2
JACEE and RUNJOB [8,9] power law fits to primary energy/nucleon spectra. Units are: $m^{-2}\,s^{-1}\,sr^{-1}\,(TeV/n)^{-1}$

el	JACEE	RUNJOB
p	$0.111^{+0.008}_{-0.006} \times E^{-2.80\pm0.04}$	$(0.103 \pm 0.006) \times E^{-2.78\pm0.05}$
He	$(7.86 \pm 0.24) \times 10^{-3} \times E^{-2.68^{+0.04}_{-0.06}}$	$(5.57 \pm 0.41) \times 10^{-3} \times E^{-2.81\pm0.06}$
CNO	$(4.11 \pm 0.41) \times 10^{-4} \times E^{-2.50\pm0.05}$	$(3.16 \pm 0.32) \times 10^{-4} \times E^{-2.65\pm0.05}$

CNO spectra have been extracted from the experimental points, because they are not reported in the literature, except for the power index (γ) of the RUNJOB spectrum ($\gamma \approx 2.65$) [27]. For CNO spectra, uncertainties of $\sigma(N_0) = 10\%$ on the absolute coefficient and $\sigma(\gamma) = \pm 0.05$ on the power index have been assumed.

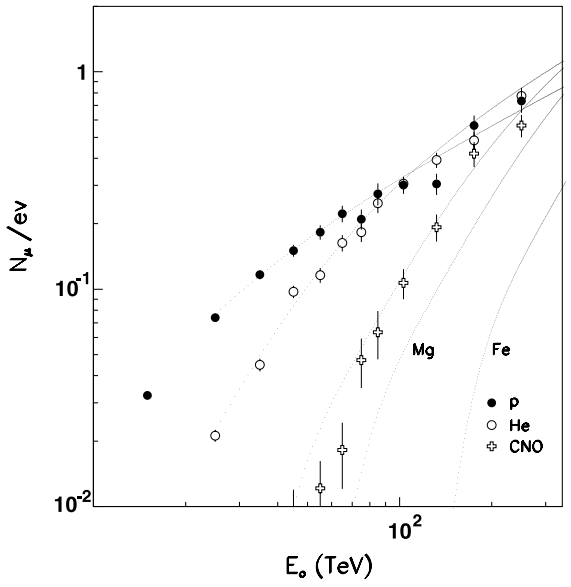

Fig. 9. Number of muons per event reaching the MACRO depth, from primary protons (full circles), He (open circles) and CNO (open crosses) as a function of primary energy. Superimposed are the results of Forti et al. [20], calculated for an effective muon threshold value $E_\mu^{\rm th} = 1.6$ TeV.

the parametrization of [20] for $\theta = 35°$. A good agreement is obtained by using as effective muon energy the value $E_\mu^{\rm th} = 1.6$ TeV, i.e., at the upper edge of the muon energy range, which accounts for a roughly 20% higher muon production efficiency of HEMAS [20] (the hadron generator uncertainties will be discussed in Section 5.2). Fig. 9 shows that the selection of primaries can be made on the basis of their energy/nucleon: at $E_0 < 40$ TeV, only primary protons have a non-negligible probability of yielding an underground muon; protons and helium primaries contribute mainly in the energy region $40 < E_0 < 100$ TeV, and CNO primaries add their contribution for $E_0 > 100$ TeV. The present analysis relies on such a selection criterion, and it allows the study of the "p + He" flux at $E_0 \approx 80$ TeV and the "p + He + CNO" one at $E_0 \approx 250$ TeV. Moreover, at energies around 80 TeV, $N_\mu^{\rm p} \approx N_\mu^{\rm He}$, and around 250 TeV, $N_\mu^{\rm p} \approx N_\mu^{\rm He} \approx N_\mu^{\rm CNO}$, indicating that in the selected energy ranges such nuclei have the same efficiency (within 15%) to yield TeV muon. The requirement of an underground muon does not distort their selected relative abundances (such differences will be accounted for in the derivations of the fluxes). In Fig. 9 the expected muon numbers for Mg and Fe primaries are also reported to show their negligible contributions.

4.3. Correlated events

The combined Cherenkov light and TeV muon simulation has been performed following the method described in [25,26]: we have considered an array of 39 identical (13×3) MACRO detectors adjacent to one another, covering an area of 230.7×158.2 m^2. The shower axis is sampled over the horizontal area of the central MACRO, and all hit detectors are considered. For each hit detector, the muon direction is obtained according to the experimental reconstruction uncertainties. The position of the shower core at the surface is recalculated as for the "real" MACRO, and the distances r from each telescope are obtained. From (A.1) (see Appendix A) the photon densities at distance r from each telescope have been sampled from Landau (central PMTs) or gaussian (lateral ones) distributions, according to the parameters reported in Table 7. The efficiency in converting photon to photoelectron densities, and the fluctuations in corresponding PMTs have been applied (see Section 3).

5. Analysis and results

5.1. Cherenkov light spectra

A first comparison between the experimental data and the expectations from the direct measurements (JACEE and RUNJOB) is obtained from the observed Cherenkov light spectra.

Convolving the probabilities per shower of producing a high energy muon ($p_{\rm p}^\mu(E_0)$, $p_{\rm He}^\mu(E_0)$ and $p_{\rm CNO}^\mu(E_0)$) with the energy spectra of p, He and CNO primaries, the rate of events $N(> E_0^{\rm th})$

recorded by MACRO as a function of the primary energy threshold ($E_0^{\rm th}$) is calculated with

$$N(>E_0^{\rm th}) = \sum_{A={\rm p,He,CNO}} (N_A > E_0^{\rm th}) = \int_{E_0^{\rm th}}^{\infty} \frac{{\rm d}N_{\rm p}}{{\rm d}E_0} \cdot p_{\rm p}^{\mu}(E_0)\,{\rm d}E_0 + \int_{E_0^{\rm th}}^{\infty} \frac{{\rm d}N_{\rm He}}{{\rm d}E_0} \cdot p_{\rm He}^{\mu}(E_0)\,{\rm d}E_0 + \int_{E_0^{\rm th}}^{\infty} \frac{{\rm d}N_{\rm CNO}}{{\rm d}E_0} \cdot p_{\rm CNO}^{\mu}(E_0)\,{\rm d}E_0. \quad (2)$$

The probabilities used in Eq. (2) have been obtained from the simulation described in Section 4.2.

In Fig. 10 the recorded integral primary energy event rates (above $E_0^{\rm th}$) as expected from the JACEE and RUNJOB data (see Table 2) are shown. Due to the strict correlation between primary energies and Cherenkov photon numbers recorded at core distances $r > 100$ m (Fig. 8), such energy event rate distributions result in distinctive C.l. photon density spectra. Therefore, the experimental integral photon density spectra are compared to the expected ones on the basis of the JACEE and RUNJOB primary CR flux measurements in different intervals of core distances. As an example, such a comparison in the region $r \in [125, 145]$ m is reported in Fig. 11. The shape of the integral spectrum is well reproduced. The experimental data are in agreement within the systematic and statistical uncertainties with the event rates based on JACEE spectra. In Fig. 12 the event rate distribution in intervals of photon density of amplitude $\Delta \log_{10}({\rm ph/m^2}) = 0.2$ is given. Such distribution is derived by scaling the measured photon densities for $r \in [145, 185]$ m following expression (A.1) to the corresponding value at $r \in [125, 145]$ m. Such scaling is straightforward in the region $100 < r < 200$ m as the l.d.f.s from p, He and CNO primaries have the same shape within 5% (see Fig. 6). While the predictions obtained with the use of the JACEE primary fluxes are consistent with the present measurements (χ^2/d.f. = 1.69) within the experimental uncertainties (mainly systematic), the predictions based on the RUNJOB fluxes underestimate the event rates (χ^2/d.f. = 5.22). This effect has to be mainly ascribed to the lower contribution of the He component in the RUNJOB data.

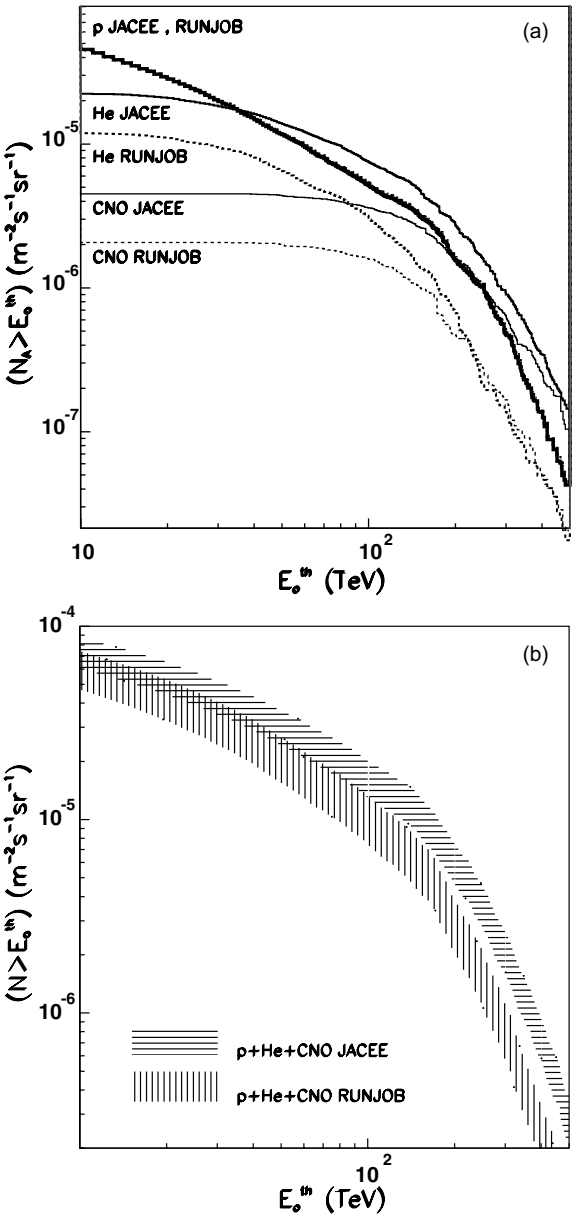

Fig. 10. Proton, helium and CNO event rates selected through the TeV muon trigger as a function of the threshold energy $E_0^{\rm th}$ (a) calculated separately, and (b) summed up together, for the JACEE and RUNJOB spectra. In plot (b) the range of intensities compatible within 1σ with the JACEE or RUNJOB fluxes are shown with dashed regions.

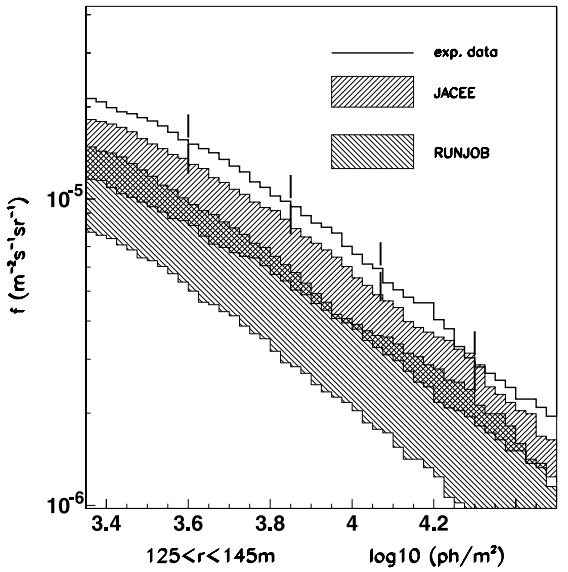

Fig. 11. Comparison between simulated (based on JACEE and RUNJOB fluxes) and experimental integral photon density spectra. Expected results using JACEE and RUNJOB fluxes inside $\pm 1\sigma$ uncertainty are indicated by dashed bands. The experimental spectrum is expressed by the thick line and the error band in $\pm 1\sigma$ by the vertical bars.

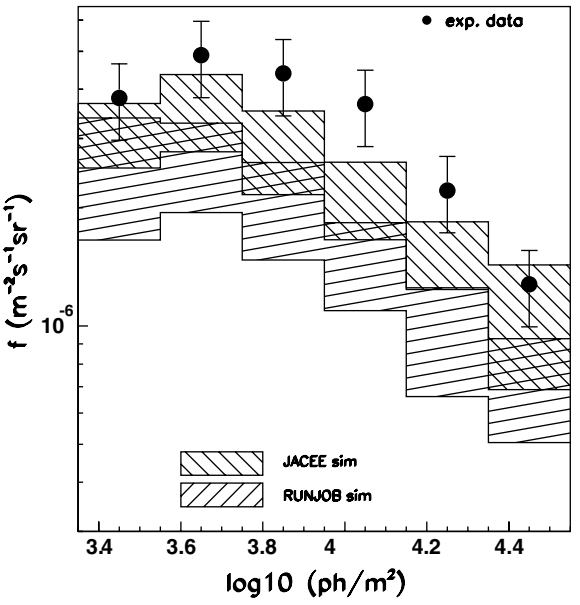

Fig. 12. Same as Fig. 11 in fixed intervals of photon density and scaling all core distances in the region $r \in [145, 185]$ m to $r \in [125, 145]$ m.

5.2. Cherenkov light lateral distribution. The hadron generator

From the integral spectra of Fig. 11, obtained at different core distances, C.l. lateral distributions have been constructed using the Constant Intensity Cut (CIC) technique (i.e., assuming that events that happen at the same rate in different distance ranges have the same energy threshold). The use of the fluxes vs. primary energy obtained by the direct measurements allows us not only to compare the shapes of the simulated and experimental curves but also to evaluate the energy related to each measured lateral distribution. The lateral distributions are measured by the number of photons corresponding to the same rates in six different coronae ($r \in [0, 20]$, $[20, 35]$, $[35, 50]$, $[125, 145]$, $[145, 165]$, $[165, 185]$ m). Due to the slightly different depths between the surface and the Gran Sasso underground laboratories at different angles, the acceptance ($A(\Upsilon, r_1, r_2)$) of each corona of every telescope (Υ) has been calculated as

$$A(\Upsilon, r_1, r_2) = \frac{N_\mu(\Upsilon, r_1, r_2)}{T(\Upsilon, r_1, r_2)} \cdot \frac{1}{I_\mu(h_\Upsilon)}, \tag{3}$$

where $N_\mu(\Upsilon, r_1, r_2)$ is the number of muon events reconstructed by MACRO in such an angular window, $T(\Upsilon, r_1, r_2)$ is the Cherenkov running time, and $I_\mu(h_\Upsilon)$ is the MACRO muon intensity, assumed constant for each telescope at its depth (h_Υ) [28].

Taking into account the error on the assumption of the constancy of $I_\mu(h_\Upsilon)$ for each telescope (6%) and the statistical error, the resulting uncertainty on the acceptances is $\sigma_A \approx 8\%$. The event rate $f_{ev}(r_1, r_2)$ is obtained as

$$f_{ev}(r_1, r_2) = \frac{\sum_{\Upsilon=1}^{5} N_{ev}(\Upsilon, r_1, r_2)}{\sum_{\Upsilon=1}^{5} A(\Upsilon, r_1, r_2) \cdot T(\Upsilon, r_1, r_2)}, \tag{4}$$

where $N_{ev}(\Upsilon, r_1, r_2)$ represents the number of coincidence events between MACRO and the EAS-TOP Cherenkov detector for the given telescope and corona.

From the simulated energy spectra associated with the photon spectra of Fig. 11, the expected event rates ($f_{ev}^{exp}(r_1, r_2)$) as a function of energy have been determined and applied to the experi-

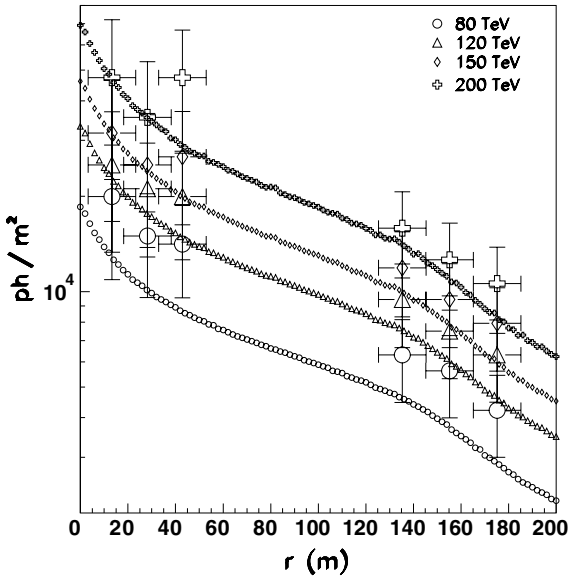

Fig. 13. Measured C.l. lateral distributions for 4 different shower energies, compared with the simulated ones using the JACEE spectra (i.e., energy–intensity relation).

mental photon spectra. Due to C.l. fluctuations in shower development the determination of the expected event rates through the integral energy spectra introduces uncertainties of 30%, 10% and 5% in the first, second and other coronae, respectively. By means of the expected event rates obtained through the procedure above described, the experimental Cherenkov light lateral distributions have been determined. Our measurement of the photon density versus the core distance for 4 different shower energies (80, 120, 150 and 200 TeV) is shown in Fig. 13. The horizontal error bars on measured points represent the uncertainty on the individual EAS core distances, while for photon densities statistical and systematic errors are added in quadrature. The experimental points are compared with the simulated lateral distribution functions, which are obtained by weighting together p, He and CNO lateral distributions according to JACEE spectra. A systematic uncertainty of about 20% has the possible effect of scaling all the curves with marginal changes to their shapes. The error on primary energy due to the uncertainty of the JACEE spectra is not included. This error is on the order of 20%, and its effect is again to scale the experimental points without changing the shapes. Within the quoted uncertainties, the calculated and experimental l.d.f.s match with each other.

Table 3
Ratio $R = ph(42)/ph(134)$ for experimental and simulated lateral distributions for different energy intervals

E (TeV)	R_{ex}	ΔR_{ex}	R_{th}
40	2.11	0.32	1.79
60	2.00	0.32	1.85
80	2.24	0.39	1.87
100	2.11	0.43	1.91
120	2.11	0.53	1.94
150	2.24	0.64	1.98
200	2.99	0.96	2.03

ΔR_{ex} represents statistical errors on experimental points.

As pointed out in [29], the slope of the C.l. lateral distribution is related to the longitudinal development of the shower. In [29], as a parameter to characterize this slope, the ratio between photon densities at 50 and 150 m from the core was introduced. By analogy, we define the ratio $R = ph(42)/ph(134)$, for which the simulated and experimental values obtained for different energies are given in Table 3. Only statistical errors are given since the systematic uncertainties cancel out in the ratio. The weighted average gives

$$\frac{R_{ex} - R_{th}}{R_{th}} = 0.14 \pm 0.09. \quad (5)$$

This value represents therefore the possible discrepancy between the expected and calculated slopes of the l.d.f.

For 60 TeV protons, the modes of the distributions of the production heights of Cherenkov photons collected at distances of 42 and 134 m are, respectively: $x_{42} = 505$ g/cm^2, and $x_{134} = 370$ g/cm^2, i.e., just around the EAS maximum.

Such C.l. lateral distribution measurements, besides providing experimental information in a region not accessible to traditional EAS measurements, confirms the good operation of CORSIKA/QGSJET in reproducing the longitudinal development of the shower at these primary energies at $(14 \pm 9)\%$ level (see Eq. (5)).

Concerning the reliability of the model in describing the high energy muon production rate: (a) the energy and kinematics ranges of interest

($\sqrt{s} = 1.7$ TeV, $Y–Y_{beam} = 5.3$) are not so far from the ones at which CORSIKA/QGSJET has been directly tested against accelerator data [30]; (b) a study performed in [31] has shown that the high energy μ production rate in p–Air collisions in the $20 < E < 200$ TeV range varies by less than 15% using different hadronic generators (QGSJET, VENUS, SIBYLL, DPMJET). We can therefore take this as an indication of the systematic uncertainties on the flux measurements due to the uncertainties of the hadronic generator code.

5.3. p, He and CNO fluxes

According to Fig. 10(a), the primary proton plus helium ("p + He") flux can be obtained in the energy range 70–100 TeV (i.e., below the threshold for CNO contribution), where the muon production efficiencies for p and He primaries (see Fig. 9), and the C.l. photons yields (for equal primary energies) are quite similar (see Fig. 8). The experimental event rate is the one inside the photon density range $10^{3.55–3.75}$ ph/m^2 (see Fig. 8). We have performed simulations of the pure proton and Helium components following the power law fits described in Section 4, considering for each component the extreme values of the spectral index (from 2.6 to 2.8), for a total of four different cases. We have restricted our selection in photon density to the bin $10^{3.55–3.75}$ ph/m^2, which corresponds to a narrow interval in energy around 80 TeV. By imposing the normalization of the simulated number of events in that bin to the experimentally detected one ($N_{ev} = 268$, see Table 4) we obtain a set of values for the flux of proton + Helium at 80 TeV ($J_{p+He}(80\ \text{TeV})$). We include the dispersion of these results in the estimate of the systematic error of the measurement of $J_{p+He}(80\ \text{TeV})$. The resulting "p + He" flux at 80 TeV is

$$J_{p+He}(80\ \text{TeV}) = (1.80 \pm 0.14^{stat} \pm 0.40^{syst}) \times 10^{-6}\,\text{m}^{-2}\,\text{s}^{-1}\,\text{sr}^{-1}\,\text{TeV}^{-1}.$$

We point out that the systematic error includes the calibration uncertainty and takes into account both the spectral index dependence and the p + He composition uncertainty, which ranges from pure p to pure He. An analogous situation (similar muon numbers and C.l. yields) holds in the energy range $E_0 = 220–300$ TeV for p, He and CNO primaries. Therefore, the same procedure described above to measure the "p + He" flux has been applied in the photon density range $10^{4.15–4.35}$ ph/m^2 to infer the "p + He + CNO" flux. Proton, helium, and CNO primaries have been simulated with extreme power law indices of primary spectra 2.8 and 2.6. The normalization to the experimental event rate (125 events) is done for the average of the six possible cases. The largest uncertainties due to different spectra and different primaries (6%) are included in the systematic uncertainties. The following flux is obtained:

$$J_{p+He+CNO}(250\ \text{TeV}) = (1.07 \pm 0.13^{stat} \pm 0.22^{syst}) \times 10^{-7}\,\text{m}^{-2}\,\text{s}^{-1}\,\text{sr}^{-1}\,\text{TeV}^{-1}.$$

Since the calibration errors affect the measurements of both "p + He" and "p + He + CNO" fluxes in the same way, their ratio is affected by a smaller systematic uncertainty. By extrapolating the "p + He" flux to 250 TeV with a 2.7 (±0.1) index of the spectrum (and taking into account an additional 12% uncertainty due to the index indeterminacy), we obtain

$$\frac{J_{p+He}}{J_{p+He+CNO}}(250\ \text{TeV}) = 0.78 \pm 0.17.$$

Table 4
Statistics of experimental events in the different photon density bins

bin ($\log_{10}$ (ph/m^2))	Number of events
2.95–3.15	38
3.15–3.35	110
3.35–3.55	213
3.55–3.75	268
3.75–3.95	246
3.95–4.15	204
4.15–4.35	125
4.35–4.55	67

6. Discussion and conclusions

A measurement of the Cherenkov light yield at different core distances in EAS in the energy range 40–300 TeV has been performed at the Gran Sasso Laboratories by the EAS-TOP and MACRO

arrays. The shower and its geometry are selected through the muons detected deep underground by MACRO ($E_\mu > 1.3$ TeV). The Cherenkov light measurements are made by EAS-TOP at Campo Imperatore (2005 m a.s.l.). The experimental data are interpreted by using simulations based on the CORSIKA/QGSJET code.

The shape of the lateral distribution reflects the rate of energy release in the atmosphere (i.e., the properties of the interaction, the primaries being dominated by the lightest components due to the TeV muon trigger requirement). Concerning this shape, simulated and real data show a good agreement, checked at the $(14 \pm 9)\%$ level, demonstrating a good description of the energy release in the atmosphere by CORSIKA/QGSJET up to above 100 TeV.

The photon density spectrum is related to the event rate, i.e., the primary proton, helium and CNO fluxes. Concerning these fluxes, as direct results of the measurement we obtain:

$$J_{\mathrm{p+He}}(80\ \mathrm{TeV}) = (1.80 \pm 0.14^{\mathrm{stat}} \pm 0.40^{\mathrm{syst}}) \times 10^{-6}\,\mathrm{m^{-2}\,s^{-1}\,sr^{-1}\,TeV^{-1}},$$

$$J_{\mathrm{p+He+CNO}}(250\ \mathrm{TeV}) = (1.07 \pm 0.13^{\mathrm{stat}} \pm 0.22^{\mathrm{syst}}) \times 10^{-7}\,\mathrm{m^{-2}\,s^{-1}\,sr^{-1}\,TeV^{-1}},$$

and hence

$$\frac{J_{\mathrm{p+He}}}{J_{\mathrm{p+He+CNO}}}(250\ \mathrm{TeV}) = 0.78 \pm 0.17.$$

The direct experiments such as RUNJOB (R) and JACEE (J) report quite similar proton fluxes in the 10–100 TeV range (the ratio of the differential spectra being $R/J = 0.97$ at 10 TeV and $R/J = 1.02$ at 100 TeV), also compatible with the flux deduced from the hadron measurements at ground level [13]. We can therefore infer the helium flux needed to be compatible with the present data by subtracting the proton flux resulting from the weighted average of the quoted results:

$$J_{\mathrm{p}}(80\ \mathrm{TeV}) = (5.3 \pm 1.1) \times 10^{-7}\,\mathrm{m^{-2}\,s^{-1}\,sr^{-1}\,TeV^{-1}}.$$

We obtain

$$J_{\mathrm{He}}(80\ \mathrm{TeV}) = (12.7 \pm 4.4) \times 10^{-7}\,\mathrm{m^{-2}\,s^{-1}\,sr^{-1}\,TeV^{-1}}$$

and

$$\frac{J_{\mathrm{p}}}{J_{\mathrm{p+He}}}(80\ \mathrm{TeV}) = 0.29 \pm 0.09.$$

The quoted errors are the combination of statistical and systematic contributions. A comparison with the existing (or extrapolated) measure- ments from JACEE and RUNJOB is given in Table 5.

While for the ratio $\frac{J_{\mathrm{p+He}}}{J_{\mathrm{p+He+CNO}}}(\approx 250\ \mathrm{TeV})$ the three measurements are quite consistent, for the He flux a better agreement is found with JACEE, with respect to which the present data are slightly higher, but consistent within the experimental (mainly systematic) uncertainties. A similar conclusion is obtained from the study of the C.l. photon density spectra, from which it results that a hard helium spectrum such as the JACEE one fits better the present data (see Figs. 11 and 12).

Table 5
Comparison (a) of the present results alone and (b) combined with the direct p-flux measurements, with the JACEE and RUNJOB data

Quantity(*)	EAS–TOP and MACRO	JACEE	RUNJOB
(a) $J_{\mathrm{p+He}}(80\ \mathrm{TeV})$	18 ± 4	12 ± 3	8 ± 2
(b) $J_{\mathrm{He}}(80\ \mathrm{TeV})$	12.7 ± 4.4	6.4 ± 1.4	3.1 ± 0.7
(b) $\frac{J_{\mathrm{p}}}{J_{\mathrm{p+He}}}(80\ \mathrm{TeV})$	0.29 ± 0.09	0.45 ± 0.12	0.63 ± 0.20
(a) $J_{\mathrm{p+He+CNO}}(250\ \mathrm{TeV})$	1.1 ± 0.3	0.7 ± 0.2	0.5 ± 0.1
(a) $\frac{J_{\mathrm{p+He}}}{J_{\mathrm{p+He+CNO}}}(250\ \mathrm{TeV})$	0.78 ± 0.17	0.70 ± 0.20	0.76 ± 0.25

CNO data and all errors of JACEE and RUNJOB are interpreted by ourselves from plots. (*)Intensity units are 10^{-7} $\mathrm{m^{-2}\,s^{-1}\,sr^{-1}\,TeV^{-1}}$.

The obtained ratio $\frac{J_p}{J_{p+He}}(80\ \text{TeV}) = 0.29 \pm 0.09$ implies that around 100 TeV the helium flux dominates over the proton one. From the ratio $\frac{J_{p+He}}{J_{p+He+CNO}}(250\ \text{TeV}) = 0.78 \pm 0.17$, it results that CNO could provide a significant contribution to the flux in the 100–1000 TeV energy region. When combined with the direct p-flux measurements, the present data imply therefore a decreasing proton contribution to the primary flux well below the observed knee in the primary spectrum. Such considerations can be described through the ratios of the three components at 250 TeV, that can be expressed as: $J_p : J_{He} : J_{CNO} = (0.20 \pm 0.08) : (0.58 \pm 0.19) : (0.22 \pm 0.17)$.

Acknowledgements

We gratefully acknowledge the support of the Gran Sasso National Laboratories and the assistance of the technical staff of the Institutions participating in the experiments. We thank Istituto Nazionale di Fisica Nucleare (INFN), the Consiglio Nazionale delle Ricerche (CNR) and the US Department of Energy and the US National Science Foundation for their support to the experiments. We also thank INFN, ICTP (Trieste), WorldLab and NATO for providing fellowships and grants (FAI) for non-Italian citizens.

Appendix A. Cherenkov light lateral distribution function and fluctuations

The average Cherenkov light l.d.f. and its fluctuations have been determined through fitting procedures of the simulated data performed at a zenith angle of 35° and requiring the presence of at least one muon with energy $E_\mu > 1$ TeV. The average photon density is represented by the following expression:

$$ph_{el}(E_0, r) = ph_{el}(E_1, r) \cdot (E_0/E_1)^{\alpha_{el}(r)} \cdot f_{el}(E_0), \tag{A.1}$$

where $ph_{el}(E_0, r)$ represents the photon density at distance r (m), E_0 (TeV) is the primary energy, el the primary. E_1 is 20 TeV for protons, 60 TeV for He and 80 TeV for CNO. $ph_{el}(E_1, r)$ are shown in Table 6 and also in Fig. 6 for the CNO component.

Some fitting functions are given in the following:

$$\alpha_p(r) = 1.27 - 0.21 \times 10^{-3} \cdot r - 0.04 \times 10^{-4} \cdot r^2,$$
$$\alpha_{He}(r) = 1.60 - 0.41 \times 10^{-3} \cdot r + 0.11 \times 10^{-4} \cdot r^2,$$
$$\alpha_{CNO}(r) = 1.43 - 0.22 \times 10^{-2} \cdot r + 0.45 \times 10^{-5} \cdot r^2.$$

$f_{el}(E_0)$ represents an ad hoc correction factor to take into account that at very low energies the lateral distribution is affected by the requirement of the TeV muon.

$$f_p = \begin{cases} 0.540 + 0.0134 \cdot E_0 - 9.55 \times 10^{-5} \cdot E_0^2 \\ \quad \text{if } E_0 < 60\ \text{TeV}, \\ 1 \quad \text{if } E_0 \geqslant 60\ \text{TeV}, \end{cases}$$

$$f_{He,CNO} = \begin{cases} 1 + 4 \times 10^{-4} \cdot (E_0 - 40) \\ \quad \text{if } E_0 < 40\ \text{TeV}, \\ 1 \quad \text{if } E_0 \geqslant 40\ \text{TeV}. \end{cases}$$

Concerning fluctuations (related to the shower development) at small core distances they can be represented for practical purposes by Landau functions (see Fig. 14) while at large distances ($r > 120$ m) gaussian shapes provide better fits (at such distances the photon densities are well related

Table 6
A partial list of $ph_{el}(E_1, r)$ values used in Eq. (A.1)

r (m)	$ph_{el}(E_1, r)$ (ph/m^2)		
	p	He	CNO
10	2056	7128	9789
20	1657	6078	8130
30	1445	5364	7169
40	1310	4910	6576
50	1192	4581	5991
60	1102	4304	5564
70	1045	4019	5348
80	975	3764	4978
90	922	3584	4806
100	877	3346	4526
110	826	3206	4273
120	792	2998	4022
130	750	2780	3727
140	707	2557	3469
150	659	2325	3105
160	591	2084	2736
170	525	1812	2374
180	463	1623	2142
190	423	1452	1901

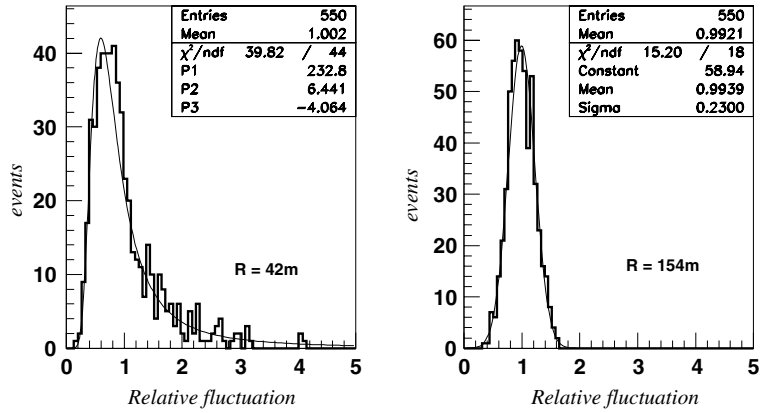

Fig. 14. Distribution of the relative Cherenkov photon density difference from the mean for 40 TeV proton showers. Distributions are fitted by Landau distributions. For increasing core distances gaussian shapes are preferred.

Table 7
Fitting parameters for the Landau and gaussian shapes (A.4)

el	E_0 (TeV)	Core distance (m)								
		Landau						Gaussian		
		[0, 20]		[20, 35]		[35, 50]		[125, 145]	[145, 165]	[165, 185]
		p2	p3	p2	p3	p2	p3	RMS	RMS	RMS
p	20	8.38	−3.35	6.37	−3.30	6.30	−3.62	0.31	0.27	0.26
p	40	7.75	−3.48	6.56	−3.71	6.44	−4.06	0.24	0.23	0.22
p	60	6.95	−3.31	6.33	−3.79	6.64	−4.21	0.22	0.20	0.21
p	80	7.07	−3.25	6.85	−4.38	6.85	−4.38	0.22	0.19	0.19
p	100	6.59	−3.31	6.89	−4.17	6.44	−4.33	0.20	0.19	0.17
p	120	6.00	−3.18	6.47	−3.99	6.96	−4.60	0.18	0.18	0.17
p	150	6.86	−3.47	6.99	−4.33	6.31	−4.36	0.18	0.17	0.17
p	200	6.14	−3.28	5.63	−3.67	6.23	−4.35	0.17	0.16	0.17
p	300	5.71	−3.27	6.40	−4.26	6.92	−4.77	0.15	0.15	0.16
He	20	6.90	−3.79	6.28	−3.95	6.68	−4.45	0.27	0.25	0.25
He	40	6.81	−3.88	6.69	−4.39	7.62	−5.13	0.23	0.21	0.21
He	60	6.33	−3.70	6.66	−4.58	8.02	−5.97	0.22	0.20	0.19
He	80	5.69	−3.39	6.63	−4.56	6.54	−4.81	0.19	0.18	0.18
He	100	4.99	−3.01	6.69	−4.52	6.64	−4.92	0.16	0.15	0.17
He	120	6.76	−3.77	7.34	−4.76	7.16	−5.13	0.16	0.15	0.15
He	150	8.60	−3.53	6.11	−4.34	6.49	−4.89	0.18	0.16	0.17
He	200	6.17	−3.92	6.44	−4.65	6.96	−5.28	0.15	0.14	0.16
He	300	6.64	−4.17	7.39	−5.34	6.89	−5.16	0.14	0.12	0.16
CNO	40	6.39	−3.95	6.78	−4.72	6.86	−5.02	0.23	0.20	0.22
CNO	60	6.20	−3.84	5.81	−4.13	6.75	−4.92	0.21	0.19	0.19
CNO	80	6.02	−3.72	6.72	−4.74	6.79	−4.98	0.20	0.18	0.18
CNO	100	5.34	−3.58	6.05	−4.75	9.17	−7.62	0.17	0.19	0.17
CNO	120	6.18	−3.98	6.74	−4.99	6.41	−5.04	0.16	0.17	0.18
CNO	150	6.22	−4.20	7.07	−5.21	6.41	−5.15	0.17	0.17	0.16
CNO	200	6.23	−4.36	6.52	−5.01	9.70	−7.82	0.15	0.14	0.14
CNO	300	5.06	−3.41	6.49	−4.67	6.77	−4.99	0.14	0.15	0.15

Errors on Landau parameters are on the order of 3–8% increasing with energy due to the lower statistics and 3–6% on the gaussian RMSs.

to the primary energies). The complete list of parameters for Landau and gaussian functions is reported in Table 7. Concerning the gaussian distributions, the quoted RMS values represent the relative dispersions.

The parameters p_2 and p_3 are related to the Landau [32] function through the expression (p_1 is the normalization factor)

$$f(x) = p_1 * \phi(\lambda), \tag{A.2}$$

$$\lambda = p_2 * x + p_3, \tag{A.3}$$

$$\phi(\lambda) = \frac{1}{2\pi \mathrm{i}} \int_{c-\mathrm{i}\infty}^{c+\mathrm{i}\infty} \mathrm{e}^{\lambda s + s \ln s}\, \mathrm{d}s. \tag{A.4}$$

In order to obtain the values reported in Table 7, the *DENLAN* function of the CERN Libraries has been used.

References

[1] B. Wiebel-Sooth et al., Astron. Astrophys. 330 (1998) 389.
[2] S. Swordy, in: Proceedings of the 23rd ICRC, Invited, Rapporteur and Highlight Papers, 1994, p. 243.
[3] A. Watson, in: Proceedings of the 25th ICRC, Invited, Rapporteur and Highlight Papers, 1998, p. 257.
[4] E.S. Seo, V.S. Ptuskin, Astrop. J. 431 (1994) 705.
[5] P.L. Biermann et al., in: H. Falcke, A. Cotera, W.J. Duschl, F. Melia, M.J. Rieke (Eds.) The Central Parsecs of the Galaxy, ASP Conference Series, vol. 186, 1999, p. 543.
[6] N.L. Grigorov, in: Proceedings of the 12th ICRC, vol. 5, 1971, p. 1746.
[7] V.I. Zatsepin, in: Proceedings of the 23rd ICRC, Invited, Rapporteur and Highlight Papers, 1994, p. 439.
[8] K. Asakimori et al. (JACEE Coll.), Astrop. J. 502 (1998) 278.
[9] A.V. Apanasenko et al. (RUNJOB Coll.), Astrop. Phys. 16 (2001) 13;
M. Furukawa et al. (RUNJOB Coll.), in: Proceedings of the 28th ICRC, vol. 4, 2003, p. 1837.
[10] H.S. Ahn et al. (ATIC Coll.), in: Proceedings of the 28th ICRC, vol. 4, 2003, p. 1833.
[11] R. Bellotti et al. (MACRO Coll.), Phys. Rev. D 42 (1990) 1396.
[12] M. Bertaina et al. (EAS-TOP & MACRO Coll.), in: Proceedings of the 27th ICRC, vol. 1, 2001, p. 14.
[13] M. Aglietta et al. (EAS-TOP Coll.), Astrop. Phys. 19–3 (2003) 329.
[14] M. Aglietta et al. (EAS-TOP Coll.), Il Nuovo Cimento 9C 2 (1986) 262.
[15] M. Aglietta et al. (EAS-TOP Coll.), Nucl. Instr. Meth. A 336 (1993) 310.
[16] M. Aglietta et al. (EAS-TOP Coll.), Il Nuovo Cimento 15C 5 (1992) 735.
[17] R. Adinolfi Falcone et al. (EAS-TOP Coll.), Nucl. Instr. Meth. A 420 (1999) 117.
[18] M. Aglietta et al. (EAS-TOP Coll.), Il Nuovo Cimento 16C 6 (1993) 813.
[19] S.P. Ahlen et al. (MACRO Coll.), Nucl. Instr. Meth. A 324 (1993) 337;
S.P. Ahlen et al. (MACRO Coll.), Phys. Rev. D 46 (1992) 4836;
M. Ambrosio et al. (MACRO Coll.), Nucl. Instr. Meth. A 486 (2002) 663.
[20] C. Forti et al., Phys. Rev. D 42 (1990) 3668.
[21] J. Knapp, D. Heck, Extensive Air Shower Simulation with CORSIKA (5.61), 1998.
[22] N.N. Kalmykov, S.S. Ostapchenko, Yad. Fiz. 56 (1993) 105.
[23] K. Bernlhöhr, Astrop. Phys. 12 (2000) 255.
[24] P. Antonioli et al., Astrop. Phys. 7 (1997) 357.
[25] G. Battistoni et al., Astrop. Phys. 7 (1995) 101.
[26] M. Aglietta et al. (EAS-TOP and MACRO Coll.), Astropart. Phys. 20 (6) (2004) 641.
[27] A.V. Apanasenko et al. (RUNJOB Coll.), in: Proceedings of the 27th ICRC, vol. 5, 2001, p. 1630.
[28] M. Ambrosio et al. (MACRO Coll.), Phys. Rev. D 52 (1995) 3793.
[29] J.R. Patterson, A.M. Hillas, J. Phys. G 9 (1983) 1433.
[30] D. Heck et al. (KASCADE Coll.), in: Proceedings of the 30th International Symposium on Multiparticle Dynamics, 2001, p. 252.
[31] G. Battistoni, Nucl. Phys. B (Proc. Suppl.) 75A (1999) 99.
[32] K.S. Kölbig, R. Schnorr, Comput. Phys. Commun. 31 (1984) 97, CERNLIB, DENLAN function, G110-1.